Volume 17 | Number 17 | 7 September 2017 | Pages 2885–2996

Lab on a Chip

Devices and applications at the micro- and nanoscale

rsc.li/loc

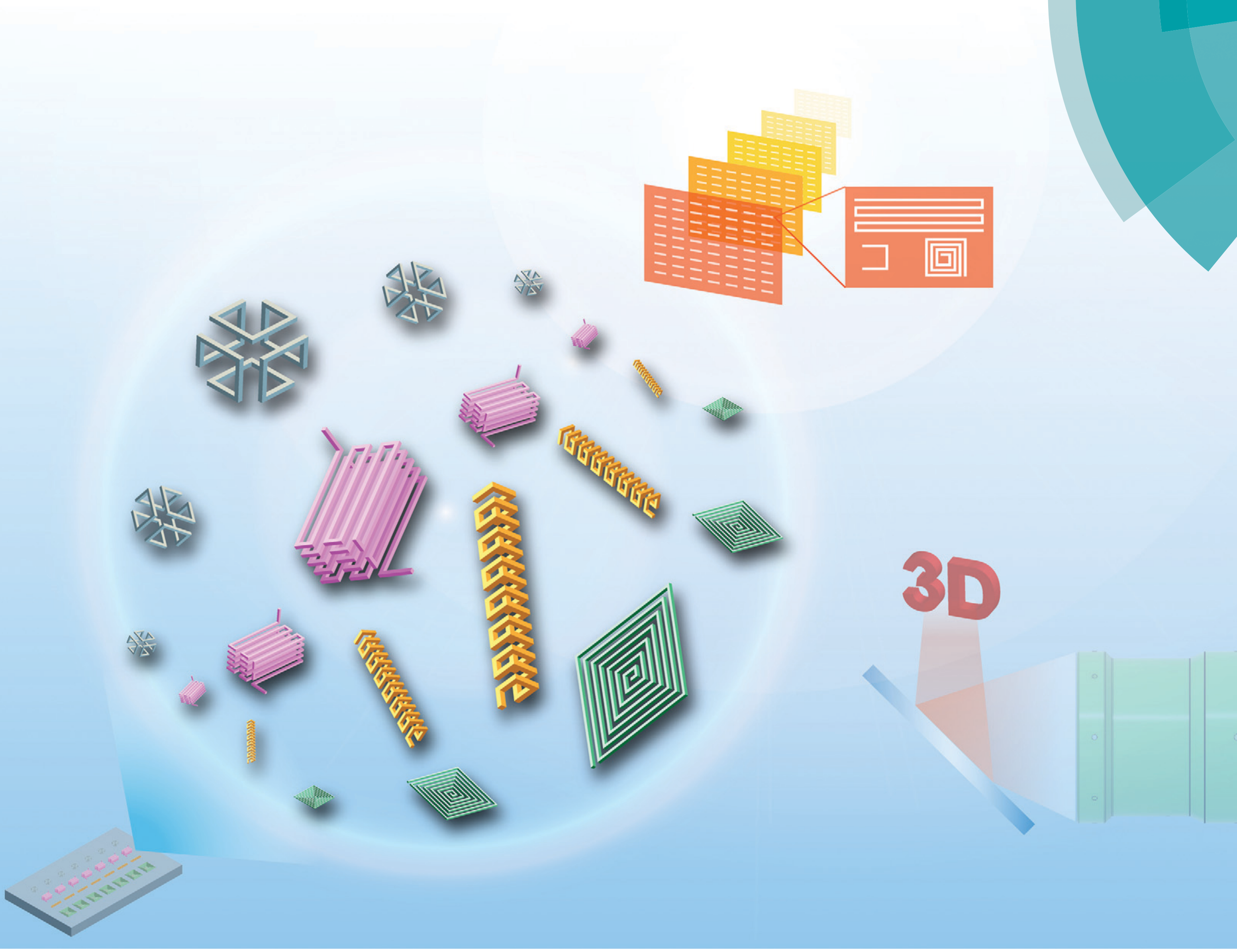

ISSN 1473-0197

ROYAL SOCIETY OF CHEMISTRY

PAPER

Gregory P. Nordin *et al.*

Custom 3D printer and resin for 18 μm × 20 μm microfluidic flow channels

Lab on a Chip

PAPER

View Article Online
View Journal | View Issue

Cite this: *Lab Chip*, 2017, **17**, 2899

Custom 3D printer and resin for 18 μm × 20 μm microfluidic flow channels†

Hua Gong,[a] Bryce P. Bickham,[a] Adam T. Woolley[b] and Gregory P. Nordin*[a]

Received 20th June 2017,
Accepted 13th July 2017

DOI: 10.1039/c7lc00644f

rsc.li/loc

While there is great interest in 3D printing for microfluidic device fabrication, to-date the achieved feature sizes have not been in the truly microfluidic regime (<100 μm). In this paper we demonstrate that a custom digital light processor stereolithographic (DLP-SLA) 3D printer and a specifically-designed, low cost, custom resin can readily achieve flow channel cross sections as small as 18 μm × 20 μm. Our 3D printer has a projected image plane resolution of 7.6 μm and uses a 385 nm LED, which dramatically increases the available selection of UV absorbers for resin formulation compared to 3D printers with 405 nm LEDs. Beginning with 20 candidate absorbers, we demonstrate the evaluation criteria and process flow required to develop a high-resolution resin. In doing so, we introduce a new mathematical model for characterizing the resin optical penetration depth based only on measurement of the absorber's molar absorptivity. Our final resin formulation uses 2-nitrophenyl phenyl sulfide (NPS) as the UV absorber. We also develop a novel channel narrowing technique that, together with the new resin and 3D printer resolution, enables small flow channel fabrication. We demonstrate the efficacy of our approach by fabricating 3D serpentine flow channels 41 mm long in a volume of only 0.12 mm^3, and by printing high aspect ratio flow channels <25 μm wide and 3 mm tall. These results indicate that 3D printing is finally positioned to challenge the pre-eminence of methods such as soft lithography for microfluidic device prototyping and fabrication.

1 Introduction

As evidenced by numerous recent reviews,[1–10] the advantages of 3D printing for microfluidic device fabrication are increasingly being recognized. Digital light processing stereolithography (DLP-SLA) is an especially attractive lower-cost 3D printing approach for microfluidics,[11,12] particularly since a microfluidic device is essentially a series of linked voids in a bulk material. During DLP-SLA fabrication, such voids are regions of unpolymerized resin that must be flushed after 3D printing, which is an easier process than trying to remove a solid sacrificial support as required by other 3D printer technologies such as polyjet.[13,14] Unfortunately, as we showed in ref. 11, current commercial 3D printing tools and materials are unable to fabricate truly microfluidic voids (<100 μm), and hence 3D printed devices are at best in the large microfluidic regime (100–500 μm),[14–20] but more often in the millifluidic (>1 mm)[13,21–23] or sub-millifluidic (0.5–1.0 mm)[24–30] regimes (see ref. 12 for a review of 3D printed microfluidics in terms of these size categories).

We recently showed that custom resin formulation in conjunction with a relatively high resolution DLP-SLA 3D printer (27 μm pixel pitch in the image plane) enabled us to 3D print microfluidic flow channels with cross sectional area (108 μm × 60 μm) near the boundary between the microfluidic and large microfluidic regimes.[11] We leveraged these advances to 3D print very compact valves and pumps, leading to the demonstration of high density integration of such components in a 3-to-2 microfluidic multiplexer with a fully 3D layout, thereby illustrating some of the advantages of 3D printing for microfluidics.[31]

In this paper, we show how 3D printing can be further extended to fabricate microfluidic flow channels with cross sectional area small enough to be in the truly microfluidic regime. Our approach is to construct our own high resolution 3D printer (7.6 μm pixel pitch in the image plane) and develop a custom resin specifically tailored to take advantage of the 385 nm LED spectrum of the 3D printer. Moreover, we introduce a new channel narrowing technique that results in reliably printing flow channels as small as 18 × 20 μm^2, which is 18 times smaller than our previous results in ref. 11. To demonstrate the efficacy of our approach, we fabricate 41 mm long 3D serpentine flow channels in a volume of only 1.56 mm × 0.38 mm × 0.21 mm = 0.12 mm^3. We also

---

[a] *Department of Electrical and Computer Engineering, Brigham Young University, Provo, UT 84602, USA. E-mail: nordin@byu.edu*

[b] *Department of Chemistry and Biochemistry, Brigham Young University, Provo, UT 84602, USA*

† Electronic supplementary information (ESI) available. See DOI: 10.1039/c7lc00644f

demonstrate high aspect ratio channels <25 μm wide and 3 mm tall. In short, we show that when appropriately applied, DLP-SLA is an effective method to 3D print truly microfluidic voids, which lays the foundation for 3D printing to challenge the dominance of conventional methods of microfluidic prototyping and development such as soft lithography and hot embossing.

2 Materials and methods

2.1 Custom 3D printer

Our two most important design criteria for constructing a custom 3D printer for microfluidics are a high resolution light engine and a UV LED light source. The former is critical to achieve small in-plane (*x*–*y*) void size, while the latter enables a wider selection of materials for custom resin formulation than the 405 nm sources we have previously worked with.[11] As we show in sect. 3.1, creating a resin with the correct optical properties relative to the light source is critical to achieve small out-of-plane (*z* dimension) void size.

Our 3D printer design is shown in Fig. 1. A schematic illustration of its layout and operation is included in Fig. S1, ESI.† The 3D printer comprises a light engine, a 45° turning mirror with 3 axes of adjustment, a 3D printing mechanism, and custom-made mounts. The light engine and turning mirror are attached to a common base, which in turn is mounted to a rail so that the assembly can be conveniently shifted between the 3D printing mechanism on the left and a resin dose calibration set up (detailed in sect. 2.4) on the right.

The light engine (Visitech, Lier, Norway) is based on a TI DLP9000 (Texas Instruments) containing a 2560 × 1600 micromirror array. With a 1:1 imaging system, the image plane resolution is 7.6 μm and the projected area is 19.35 × 12.10 mm^2. The optical source in the light engine is a 385 nm LED. We measure the peak wavelength and full-width at half-maximum (FWHM) of the source to be 383.4 nm and 12.6 nm, respectively. The 45° turning mirror reflects light from the horizontally mounted light engine such that projected patterns can be focused through the transparent bottom of a resin tray. We heavily modified a Solus 3D printing mechanism (Junction3D, Santa Clarita, CA) to serve as a platform for the 3D printing process. The bottom of the resin tray is a replaceable Teflon film that is tensioned on an underlying quartz window to guarantee flatness.

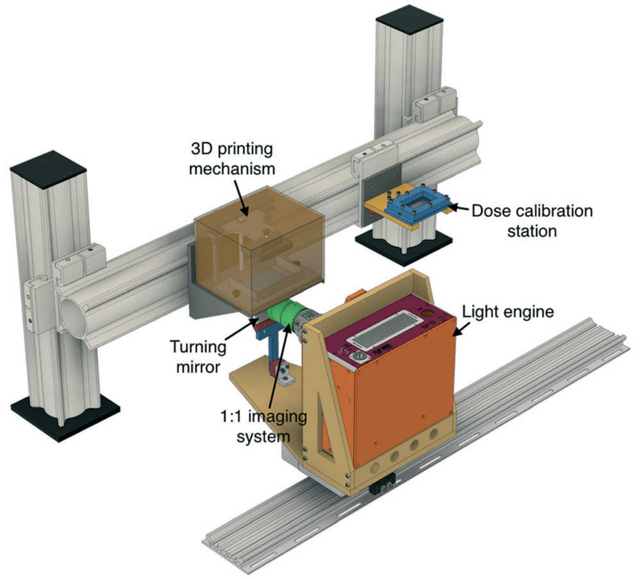

Fig. 1 3D CAD model of our custom 3D printer.

In its current configuration, the ultimate build size of our 3D printer is 19.35 mm × 12.10 mm × 80 mm, where the XY size and the Z size are determined by the projected image from the light engine and the Solus mechanism, respectively. Note that we have deliberately traded-off XY size in favor of higher XY resolution, which is required to obtain small in-plane void size. If desired, the XY build size can be increased without compromising resolution by exposing multiple images side-by-side for each layer. This can be accomplished, for example, by translating the light engine in XY. In this paper we use a single image position for each layer, and defer translating the light engine to future work.

We have developed custom Python software to operate our 3D printer. The software controls the 3D printing mechanism over a serial channel using G-code and the light engine over I^{2}C to a low-level hardware interface. Images are sent with a graphics card through HDMI. All synchronization of 3D printer functions is performed in the Python code. The code gives us absolute control over all aspects of the 3D printer, including arbitrary exposure times for arbitrary layers during a 3D print, multiple independent exposures per layer, variable layer thicknesses, and, most importantly, single pixel precision in the projected images.

2.2 Materials

The focus of our resin formulation efforts is finding one or more UV absorbers that will give the optical properties needed to achieve small void size in the *z* dimension. Similar to our previous work,[11,19,31] we use poly(ethylene glycol) diacrylate (PEGDA, MW258) as the monomer and phenylbis(2,4,6-trimethylbenzoyl)phos-phine oxide (Irgacure 819) as the photoinitiator. They are obtained from Sigma-Aldrich (St. Louis, MO) and BASF (Vandalia, Illinois), respectively.

Part of the motivation for use of a PEGDA-based resin is that we have already shown[32] that it has low non-specific adsorption and is suitable for electrophoretic separations. Moreover, Urrios *et al.* showed that their PEGDA resin formulation could be made biocompatible with a specific post-processing treatment.[33] Regarding solvent compatibility, we have found 3D printed PEGDA resins to be compatible with some solvents such as isopropyl alcohol and ethanol, but not others such as acetone and toluene.

As indicated in Fig. 2, we evaluate 20 potential UV absorbers. Their molecular structures are shown in Fig. S2, ESI.† Nearly all are inexpensive and readily available. The

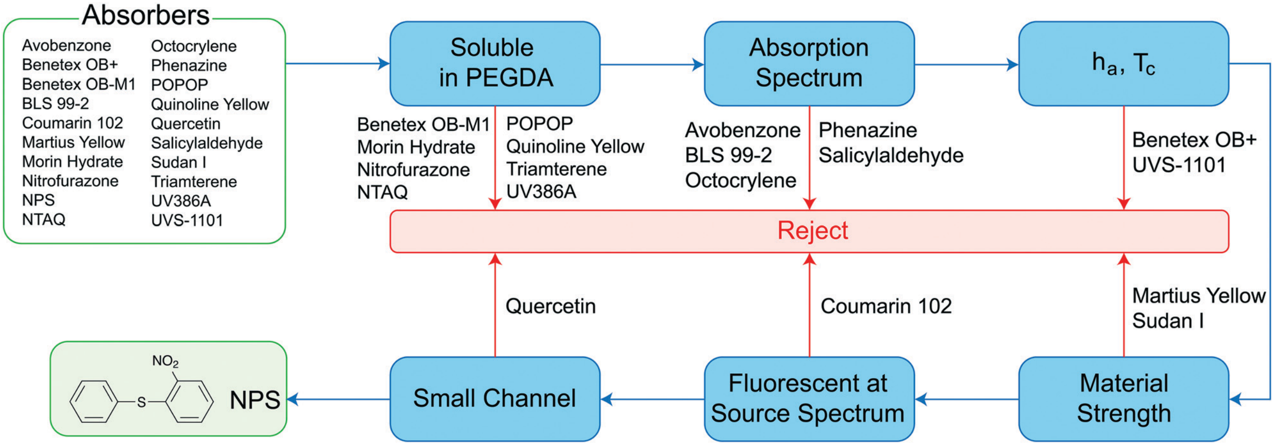

Fig. 2 UV absorber evaluation criteria and process flow. 20 absorbers are initially considered. Rejected absorbers are indicated at each step in the process where they do no pass the evaluation criterion.

absorbers are avobenzone, 2,5-bis(5-*tert*-butyl-benzoxazol-2-yl)thiophene (Benetex OB+), disodium 4,4′-bis(2-sulfonatostyryl)biphenyl (Benetex OB-M1), benzenepropanoic acid (BLS 99-2), 2,3,6,7-tetrahydro-9-methyl-1*H*,5*H*-quinolizino-(9,1-gh)coumarin (Coumarin 102), Martius Yellow, morin hydrate, nitrofurazone, 2-nitrophenyl phenyl sulfide (NPS), 5,12-naphthacenequinone (NTAQ), octocrylene, phenazine, 1,4-bis-(2-(5-phenyloxazolyl))-benzene (POPOP), quinoline yellow, 3,3′,4′,5,6-pentahydroxyflavone (Quercetin), salicylaldehyde, Sudan I, triamterene, UV386A, and 9,10-diethoxyanthracene (UVS-1101). Avobenzone and octocrylene are purchased from MakingCosmetics (Snoqualmie, WA); Benetex OB+, Martius Yellow, morin hydrate, quinoline yellow, quercetin, and Sudan I from Sigma-Aldrich (St. Louis, MO); Benetex OB-M1, nitrofurazone, and NPS from TCI America (Portland, OR); Coumarin 102, triamterene, and UVS-1101 from Alfa Aesar (Haverhill, MA); BLS 99-2 from Mayzo (Suwanee, GA); NTAQ and phenazine from Santa Cruz Biotechnology (Dallas, TX); salicylaldehyde from Thermo Fisher Scientific (Waltham, MA); and UV386A from QCR Solutions (St. Lucie, FL). Each chemical is used as received.

Resins studied for 3D printing are prepared by mixing 1% (w/w) Irgacure 819 and the desired concentration of UV absorber with PEGDA, and sonicating for 30 min. All photoinitiator-containing resins are stored in amber glass bottles after mixing.

2.3 Molar absorptivity measurement

The absorption spectrum of each UV absorber is measured by mixing the absorber at a specific concentration with PEGDA and placing a drop of resin in the gap between a glass slide and a coverslip separated by 65 μm spacers. The resin is illuminated through the glass slide with attenuated light from a broadband XCITE-120Q source (Lumen Dynamics, Ontario, Canada). The transmitted light is captured by a fiber with 100 μm diameter core connected to a QE65000 spectrometer (Ocean Optics, Dunedin, FL). The molar absorptivity is calculated from the measured absorption spectra of resins with and without an absorber, and from the known resin thickness.

2.4 Dose calibration

Polymerization thickness as a function of optical dose is measured with the set up on the right in Fig. 1, which consists of a custom resin container with a 75 × 50 mm^2 glass window in the bottom. When the light engine is shifted on the rail to this calibration station, the height of the resin container is adjusted so that the projected image is focused on the top surface of the window. A layer of resin ~1 mm thick is applied to the window and exposed to a series of 1 mm^2 square patterns with different exposure times, which results in different polymerization depths. After rinsing unpolymerized resin with isopropyl alcohol (IPA), we measured the thickness of the polymerized regions using a Zeta-20 3D optical profilometer (Zeta Instruments, San Jose, CA).

2.5 3D printing

3D prints are fabricated on diced and silanized glass slides. The silanization procedure is given in ref. 31, except that in the present work we use a silane concentration of 10% rather than 2%. All 3D prints are exposed with a measured optical irradiance of 21.2 mW cm^{-2} in the image plane.

2.6 Material mechanical properties

As discussed in sect. 3.2, we experimentally observe that some UV absorbers appear to hinder the photopolymerization process such that a given dose results in noticeably different material strengths for different absorbers. To illustrate this phenomenon, we measure the hardness and Young's modulus of two resins containing different UV absorbers. Measurements are made with 19.35 × 12.10 × 5 mm^3 3D printed blocks of polymerized resin printed with a 5 μm layer thickness. Their Shore hardness is measured with a Rex Gauge Model 1600 durometer (Buffalo Grove, IL) for both ASTM D2240 Type A and Type D scales. The Young's Modulus is measured in compression with an Instron 3455 (Instron, Norwood, MA).

2.7 Post-print curing

In our previous paper,[31] 0.01% w/w azobisisobutyronitrile (AIBN) was added to the resin to enable post-print thermal curing to drive further polymerization and obtain improved mechanical properties. However, we find that the 385 nm source of our new 3D printer activates AIBN such that it is consumed during 3D printing, and is therefore unavailable for post-print thermal curing. We tried an alternate thermal initiator, benzoyl peroxide, but found that it was likewise activated during 3D printing. Therefore, we employ an optical curing approach in this paper. The key is to use a photoinitiator with absorbance that extends to longer wavelengths than the long wavelength cut off of the UV absorber such that light in this region penetrates through the device. For example, in Fig. 3(a), the Irgacure 819 absorption spectrum extends to ~460 nm, while NPS and Martius Yellow drop off at ~440 nm. For post-print optical curing we use an inexpensive consumer UV nail curer (54 Watt Professional UV Nail Dryer, Royal Nails) that emits a broad spectrum.

3 Results and discussion

In this section we begin by stepping through the process of developing a custom resin to fabricate truly microfluidic void sizes based on our new 3D printer, taking into account the source and UV absorber spectra. We develop a mathematical model from which the optical penetration depth for a resin, h_a, can be calculated directly from its measured molar absorptivity and desired absorber concentration, and also determine h_a and the critical exposure time, T_c, (see ref. 11 for the model details) from experimental measurement of polymerization thickness as a function of exposure time. Our assessment leads to the selection of NPS as the UV absorber for our resins. Next, we evaluate the minimum achievable void size as a function of layer thickness and layer exposure time for 2% w/w NPS concentration. Using calculated dose as a function of z, we develop a model for the minimum achievable void size, and demonstrate that the model is predictive by applying it to 3% NPS resin to obtain flow channels with a design height of 18 μm. We then introduce a new channel narrowing technique that reduces channel width from ~38 μm to ~20 μm. Finally, we demonstrate the utility of our methods by fabricating 41 mm long 3D serpentine flow channels and high aspect ratio flow channels.

3.1 Absorber selection

3.1.1 Criteria. Our approach to evaluating UV absorber candidates is illustrated in Fig. 2, which we apply to 20 candidate absorbers. These candidates were primarily found by examining chemical manufacturer websites and manually assessing absorption spectra in the 20 volumes of ref. 34.

Most UV absorbers are powders that must be mixed with PEGDA, a liquid. The first test criterion is therefore whether

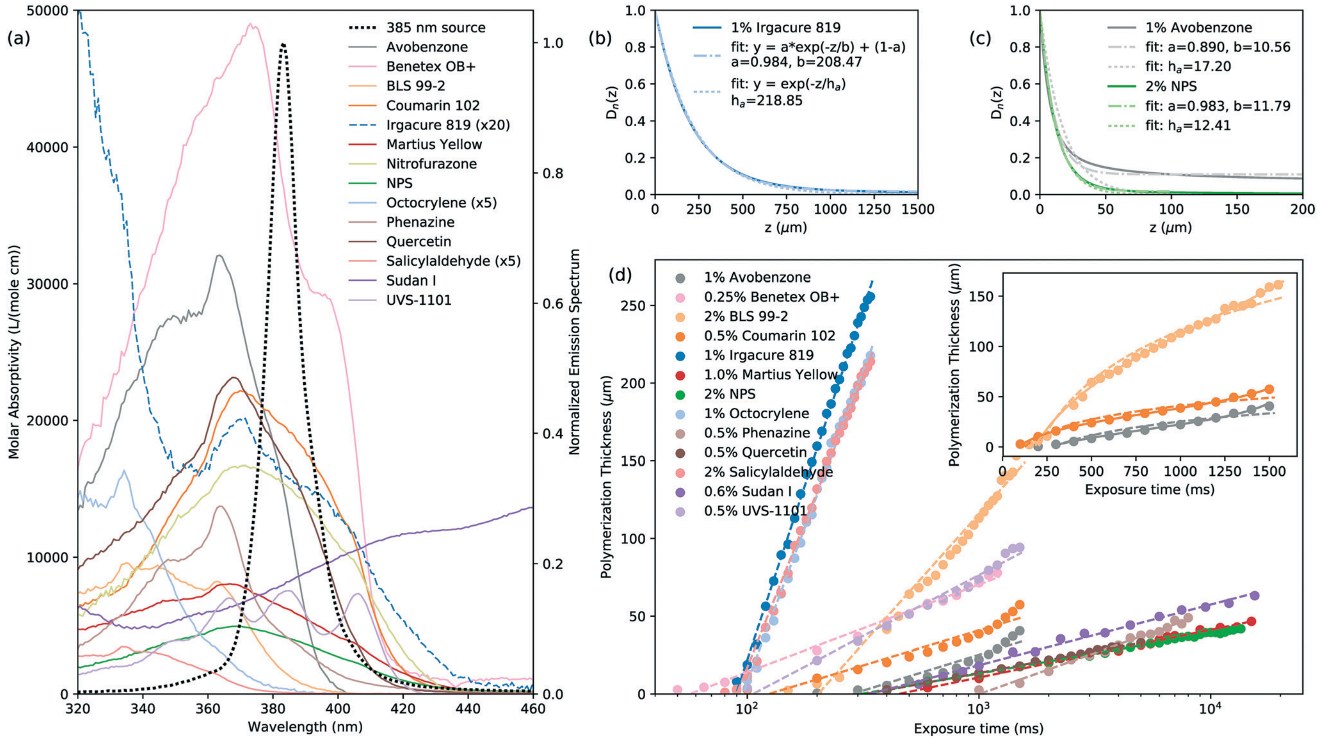

Fig. 3 (a) Measured molar absorptivity and LED source spectrum. (b) $D_n(z)$ calculated from molar absorptivity for 1% Irgacure 819 resin. (c) Same as (b) except for 1% Avobenzone and 2% NPS resins. (d) Measured polymerization thickness as a function of exposure time for 13 resins. Each resin contains 1% Irgacure 819 in addition to the specified UV absorber. Dashed lines indicate fit to model 3. Inset shows that model 4 (solid lines) is a better fit for some resins.

the absorber is soluble. Table 1 shows the results of our solubility measurements. Seven of the 20 candidate absorbers are found to be insoluble in PEGDA and an eighth, nitrofurazone, has such a low solubility (0.07%) that it is unusable.

The next criterion is whether the absorber's absorption spectrum fully overlaps the emission spectrum of the light engine optical source. Fig. 3(a) shows the measured molar absorptivity as a function of wavelength for the remaining absorber candidates. It also shows the molar absorptivity of the photoinitiator, Irgacure 819, and the light engine source spectrum. As is evident from the figure, 5 absorber candidates have poor spectral overlap with the source. In each case, the absorber's long wavelength tail is insufficient to cover the full source spectrum. The result is that some of the source spectrum will penetrate deeper into the device during 3D printing, causing unpolymerized resin in what should be voids to polymerize and thereby fill the voids. Such absorbers are therefore incapable of being used to fabricate small voids, as we show below.

3.1.2 Mathematical model. In ref. 11 we noted that the polymerization depth, z_p for an exposure time of t_p is

$$z_\mathrm{p} = h_\mathrm{a} \ln \frac{t_\mathrm{p}}{T_\mathrm{c}} \tag{1}$$

where $h_\mathrm{a} = 1/\alpha$ and α is the resin's absorption coefficient. This result assumes monochromatic illumination, which is valid if the absorption coefficient is relatively constant over the source spectrum. However, in this paper we consider wavelength-dependent absorption such that we need to develop a more refined model.

Consider a photopolymerizable resin with absorption coefficient $\alpha(\lambda)$ occupying the half space $z \geq 0$ and illuminated by a polychromatic light source, $I_0(\lambda)$, from the $-z$ direction. The dose (J cm^{-2}) at z for exposure time t can be expressed as (see sect. S3, ESI† for a comprehensive comparison of the monochromatic and polychromatic cases).

$$D(z,t) = t\int_0^\infty I_0(\lambda)\mathrm{e}^{-\alpha(\lambda)z}\mathrm{d}\lambda. \tag{2}$$

Normalizing by the dose at $z = 0$ we obtain,

$$D_\mathrm{n}(z) = \frac{D(z,t)}{D(0,t)} \tag{3}$$

$$= \frac{\int_0^\infty I_0(\lambda)\mathrm{e}^{-\alpha(\lambda)z}\mathrm{d}\lambda}{\int_0^\infty I_0(\lambda)\mathrm{d}\lambda}. \tag{4}$$

The normalized dose, $D_\mathrm{n}(z)$, indicates how rapidly the relative dose decreases as a function of z, and has the functional form of a weighted average of $\mathrm{e}^{-\alpha(\lambda)z}$ over λ with weighting function $I_0(\lambda)$. Based on many calculations with measured spectra for numerous absorbers, we have found that this weighted average can be approximated as

$$D_\mathrm{n}(z) \approx a\mathrm{e}^{-z/b} + c \tag{5}$$

$$= 1 - a(1 - \mathrm{e}^{-z/b}), \tag{6}$$

where we have used $c = 1 - a$ in eqn (6), which can be derived from $D_\mathrm{n}(0) = 1$. When there is good spectral overlap between an absorber and the source spectrum, $a = 1$ and the approximation for $D_\mathrm{n}(z)$ reduces to

$$D_\mathrm{n}(z) \approx \mathrm{e}^{-z/h_\mathrm{a}}, \tag{7}$$

where we have recognized that $b = h_\mathrm{a}$. We refer to eqn (7) as model 1 and eqn (6) as model 2. Both depend solely on the spectral properties of the absorber and the source. Given the molar absorptivity, $\varepsilon(\lambda)$, from Fig. 3(a), the absorption coefficient, $\alpha(\lambda)$, is

$$\alpha(\lambda) = \log(10)\varepsilon(\lambda)C \tag{8}$$

where the molar concentration, C, can be calculated from the w/w absorber concentration, $C_\mathrm{w/w}$, in percent as

$$C = \frac{C_\mathrm{w/w}}{100}\frac{\eta_\mathrm{P}}{M_\mathrm{a}} \tag{9}$$

in which η_P is the density of PEGDA and M_a is the absorber molar mass.

Fig. 3(b) and (c) show example calculations of $D_\mathrm{n}(z)$ using eqn (4) and (8) for three resins based on their measured absorption spectra and the light engine source spectrum. As seen in Fig. 3(a), both Irgacure 819 and NPS have good

Table 1 Solubility in PEGDA and fluorescence with 385 nm excitation. Dash indicates insolubility

Material	Solubility (%)	Fluorescent
Avobenzone	>5	
Benetex OB+	0.25	Yes
Benetex OB-M1	—	Yes
BLS 99-2	>5	
Coumarin 102	0.8	Yes
Irgacure 819	>5	
Martius Yellow	3	
Morin hydrate	—	
Nitrofurazone	0.07	
NPS	>5	
NTAQ	—	
Octocrylene	>5	
Phenazine	1.8	
POPOP	—	Yes
Quercetin	0.8	
Quinoline yellow	—	
Salicylaldehyde	>5	
Sudan I	2.7	
Triamterene	—	Yes
UV386A	—	
UVS-1101	0.5	Yes

spectral overlap with the source spectrum, such that fitting model 2 to the calculated $D_n(z)$ yields a very close to 1, in which case b from model 2 and h_a from model 1 agree to within 5%. On the other hand, avobenzone does not have good spectral overlap with the source such that $a < 0.9$, and b and h_a differ by 60%. Note that for Irgacure 819 and NPS, $D_n(z) \rightarrow 0$ as $z \rightarrow \infty$, whereas for avobenzone $D_n(z) \rightarrow \sim 0.1$. Hence at depths beyond several h_a, NPS resin will remain largely unexposed, whereas avobenzone resin will continue to photopolymerize, making it unusable to fabricate small voids.

3.1.3 Polymerization as a function of dose. In ref. 11 we utilized a resin characterization method in which the polymerization thickness is measured for a series of exposure times, followed by fitting the data to eqn (1) to determine h_a and T_c. We employ a similar method in this paper, except that when there is poor spectral overlap between the absorber and the source spectrum, the polymerization behavior is better modeled by

$$t_p = \frac{T_c}{(1-a) + a\exp(-z_p/b)} \tag{10}$$

(see sect. S4, ESI† for derivation). We refer to eqn (1) as model 3 and eqn (10) as model 4. These models' fit parameters are based solely on measured polymerization thickness as a function of optical exposure time.

Fig. 3(d) shows the measured polymerization thickness as a function of exposure time for a wide selection of custom resins. In each case, the corresponding dashed line shows the fit to model 3. The inset graph also shows the fit to model 4 as solid lines for the three resins that have the poorest fit to model 3 (1.0% avobenzone, 2% BLS 99-2, and 0.5% Coumarin 102).

The fits to models 1–4 for all of the resins are shown in Table S2, ESI.† When the fit for a in models 2 or 4 is ~1, the absorber has good spectral overlap with the source. In this case models 1 and 3 are valid and typically show good agreement with each other even though they are generated from completely different measurements, thereby indicating the consistency of our analysis methods.

In addition to good spectral overlap, we also require that h_a be suitably small in order to realize 3D printed channels with small vertical void size. We therefore restrict our choice of absorbers to those that can achieve the smallest h_a, which, in conjunction with previous criteria, limits the possible absorbers to Coumarin 102, Martius Yellow, NPS, Quercetin, and Sudan I.

3.2 Material properties and layer dose

For a given irradiance and build layer thickness, the layer exposure time determines the dose and hence the degree of crosslinking in a layer. Smaller layer exposure times result in less crosslinking and hence less overall hardness and smaller Young's modulus. On the other hand, longer exposure time yields greater hardness and Young's modulus, but increases the exposure of resin in regions intended to be voids, thereby limiting the minimum vertical void size that can be achieved. There is thus a layer exposure time trade-off between material properties and minimum vertical void size. A resin that achieves adequate material properties with a smaller layer exposure time will yield a smaller vertical void size than a resin that requires a longer layer exposure time to obtain the same material properties.

As an example of the effect of two absorbers on material properties as a function of layer exposure time, consider 2% NPS and 1.2% Martius Yellow resins, which have h_a values of 11.2 and 9.8 μm, respectively. Table 2 shows the results of Young's Modulus and Type A and D Shore durometer measurements. For 2% NPS, a layer exposure time of 280 ms yields a somewhat harder and stiffer material than a 500 ms layer exposure time for 1.2% Martius Yellow. When the materials undergo the same length post-print cure, the NPS resin still has greater hardness and Young's modulus. We therefore expect to achieve significantly smaller vertical void size with the NPS resin, which is consistent with our experimental observations.

In our experience making 3D printed valves and pumps,[31] post-print curing is necessary for long valve and pump operational lifetime. Since optical curing is necessary for the reasons discussed in sect. 2.7, Sudan I is eliminated from consideration because its absorption spectrum extends far beyond the long wavelength limit of Irgacure 819 such that it

Table 2 Comparison of Young's modulus and durometer measurements for NPS and Martius Yellow resins. Durometer measurements are unitless and Young's modulus, *E*, is in MPa

2% NPS				1.2% Martius Yellow			
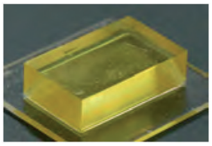				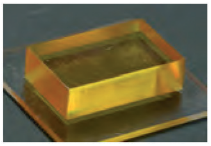			
t_{exp} (ms)	*A*	*D*	*E*	t_{exp} (ms)	*A*	*D*	*E*
280	86	21	3.5	500	84	—	2.7
400	94	52	6.6	1000	93	70	6.7
280 cured	97	75	7.7	500 cured	94	47	5.5

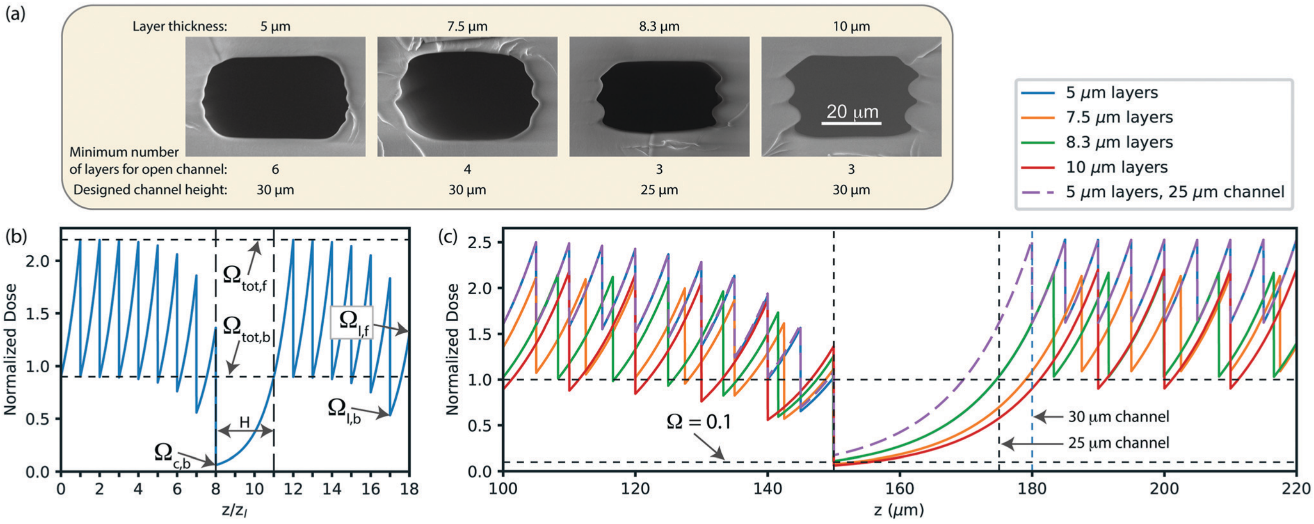

Fig. 4 (a) SEM images of flow channel cross sections for 2% NPS. See text for details. All channels are designed to be 4 pixels wide. Larger layer thickness results in larger vertical wall surface relief. (b) Normalized dose as a function of normalized depth. (c) Calculated dose as a function of depth for the cases in (a).

cannot be optically cured to achieve good material properties.

3.3 Small cross section channels

Our ultimate criterion for absorber selection is which absorber(s) result in the smallest cross section channels. Experimentally we find that Coumarin 102 can yield small channels only when they are close to the last exposed layer; deeper channels are always closed. We ascribe this to the fact that Coumarin 102 is fluorescent at 385 nm. Since fluorescent light is emitted at longer wavelengths than the excitation light, and much of it is beyond the long wavelength cutoff of Coumarin 102 absorption, the fluorescent light can penetrate

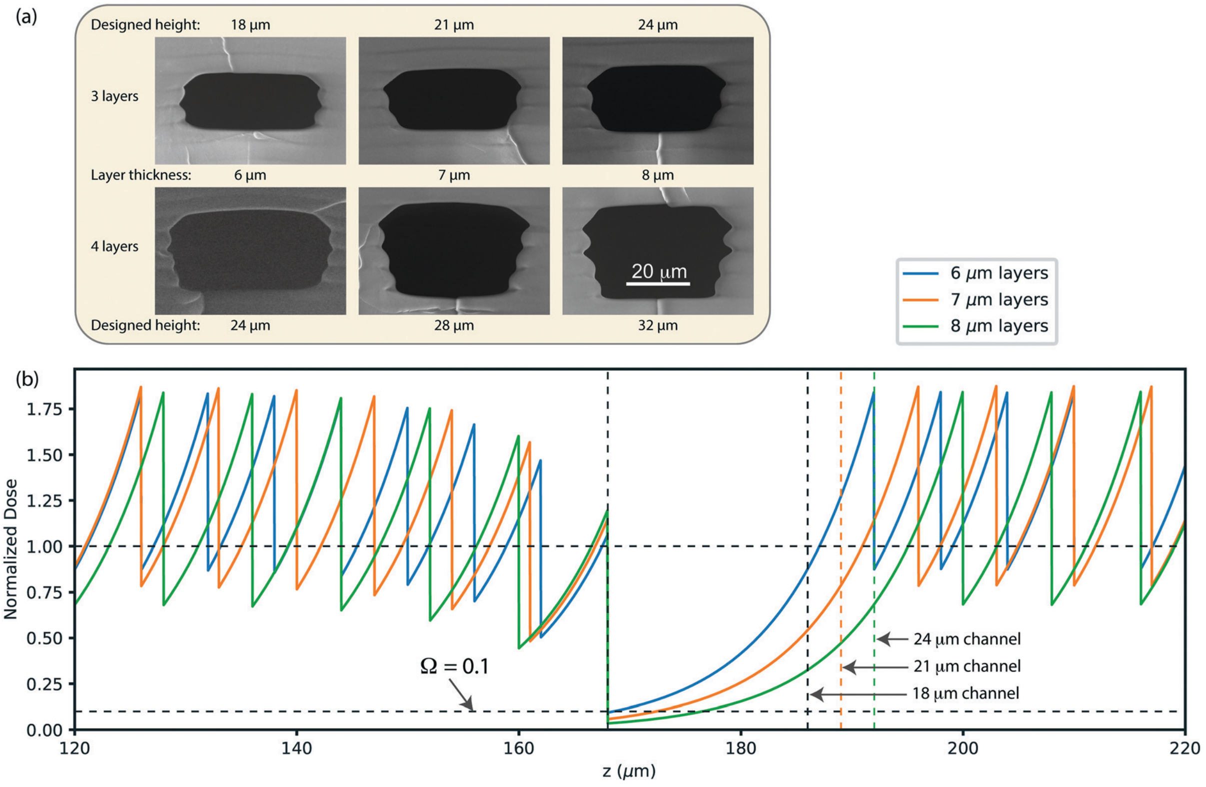

Fig. 5 (a) Same as Fig. 4(a) except for 3% NPS. (b) Calculated normalized dose as a function of depth for the 3 layer cases in (a).

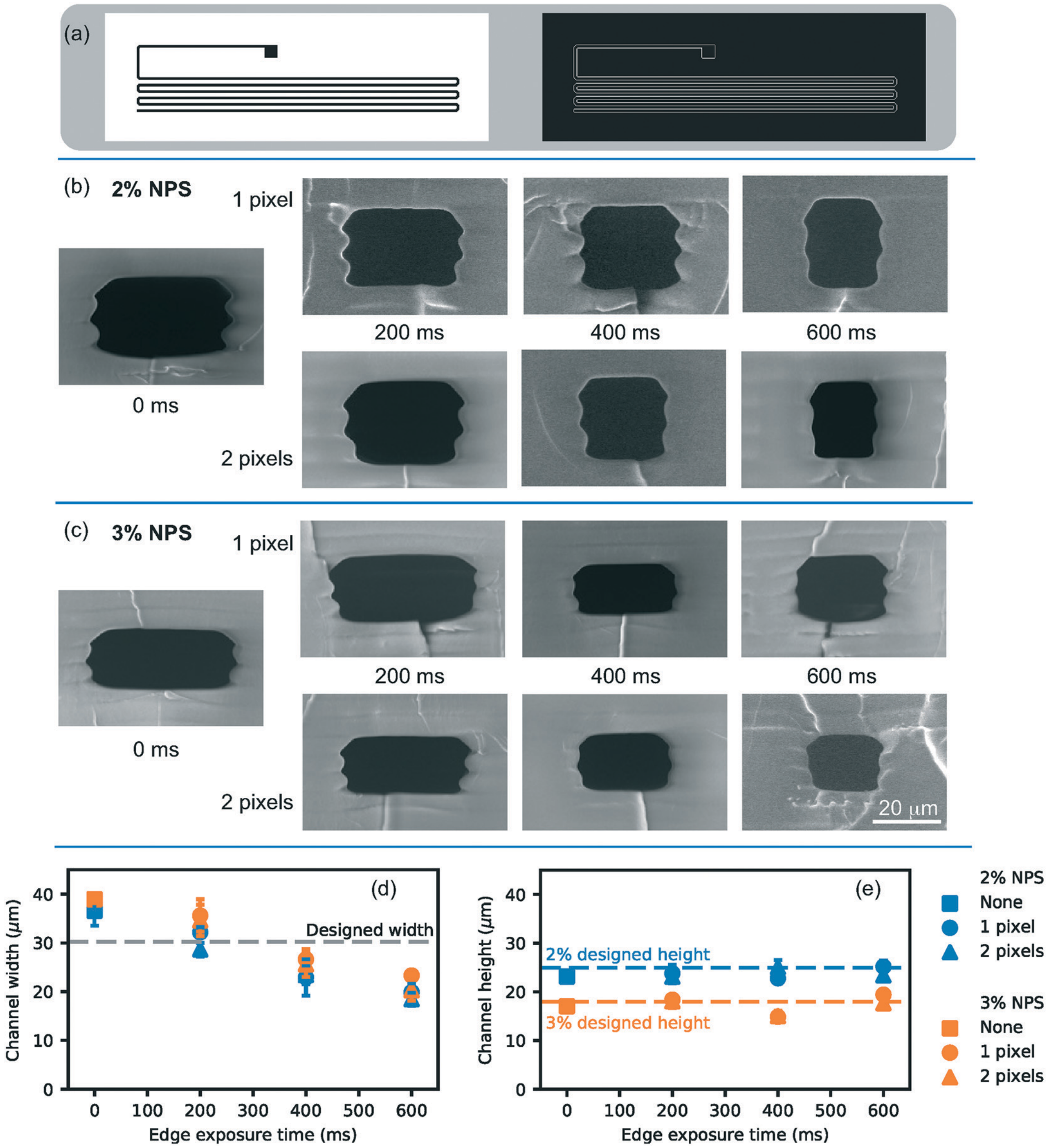

Fig. 6 (a) Primary and additional edge exposure patterns for a single layer containing a flow channel. (b) Channel narrowing for 2% NPS resin for additional edge exposure. The build layer thickness is 8.3 μm and the designed flow channel height is 25 μm. (c) Same as (b) except for 3% NPS resin with 6 μm layers and a designed flow channel height of 18 μm. (d), (e) measured channel width and height, respectively, as a function of edge exposure time.

deeper during printing such that resin in underlying channels is exposed and polymerized. Resin in channels near the surface do not receive enough dose from fluorescence in subsequent layers to become polymerized.

In the case of Quercetin, we found that small channel sizes could be fabricated, but they exhibited internal delamination. While it may be possible to find conditions in which this does not occur, we chose to focus our efforts on the remaining absorber, NPS.

3.3.1 Channel height. Extensive testing with 2% NPS reveal a set of conditions that repeatably result in the smallest possible channel height with essentially 100% yield. This can be illustrated with Fig. 4(a), in which scanning electron microscope (SEM) images of channel cross sections are shown for the smallest achievable channel height (30 μm) for layer thicknesses, z_l, of 5, 7.5, and 10 μm. For 8.3 μm layers, the smallest channel height is 25 μm. A plot of normalized dose as defined in ref. 11 ($\Omega = D(z)/D_c$) is shown as a function of z/z_l for a generic case in Fig. 4(b) for the layers surrounding a flow channel intended to occupy layers 8–10. The normalized dose at the top of the channel is $\Omega_{\text{tot,b}}$, which exponentially decays through the thickness of the channel. Successful channel formation requires that this exponential tail is small enough to avoid significant polymerization of resin in the channel.

Fig. 4(c) shows the calculated normalized dose for the actual experimental conditions of Fig. 4(a). An additional example case is shown for a 25 μm channel made with 5 μm

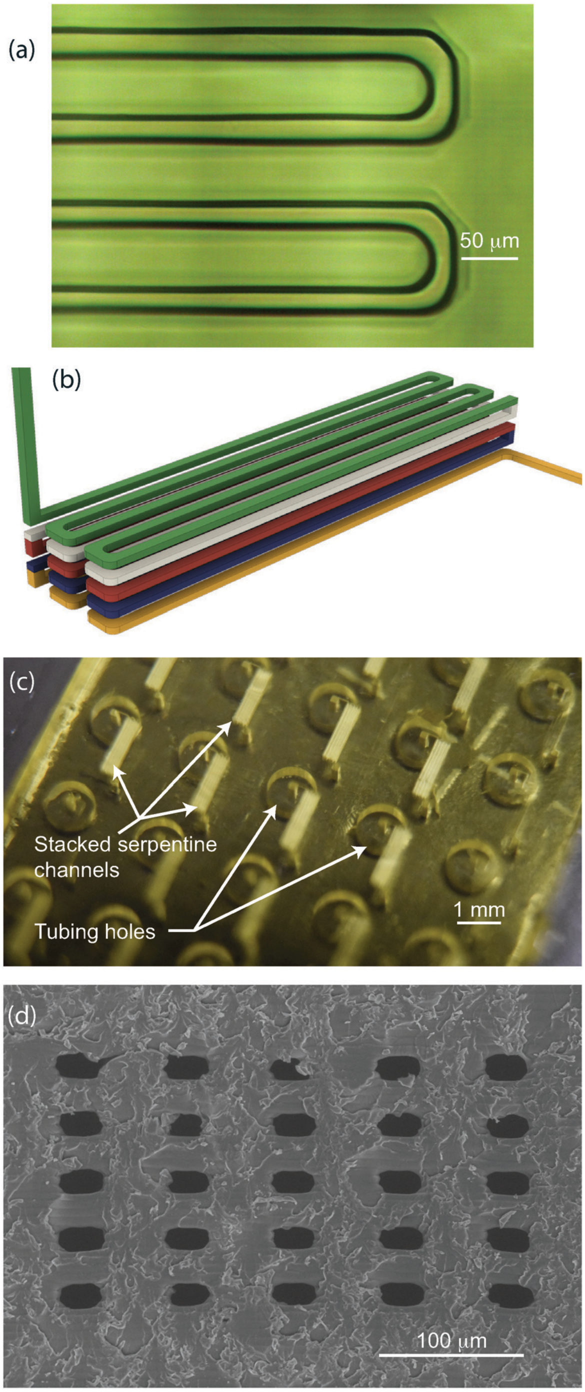

Fig. 7 (a) Microscope photograph of single layer serpentine channel. (b) Schematic illustration of 3D stacked serpentine channel design. Each layer is shown as a different color. (c) Photograph of 3D printed device with 24 3D serpentine channels. The photo is taken through the glass slide on which the device is 3D printed. (d) SEM image of 3D serpentine channel cross section.

layers, which never successfully forms clear channels. It is representative of many other parameter combinations that also fail. Experimentally, we find that the minimum height channel for a given layer thickness fufills the following conditions: (1) the normalized dose at the back of the channel,

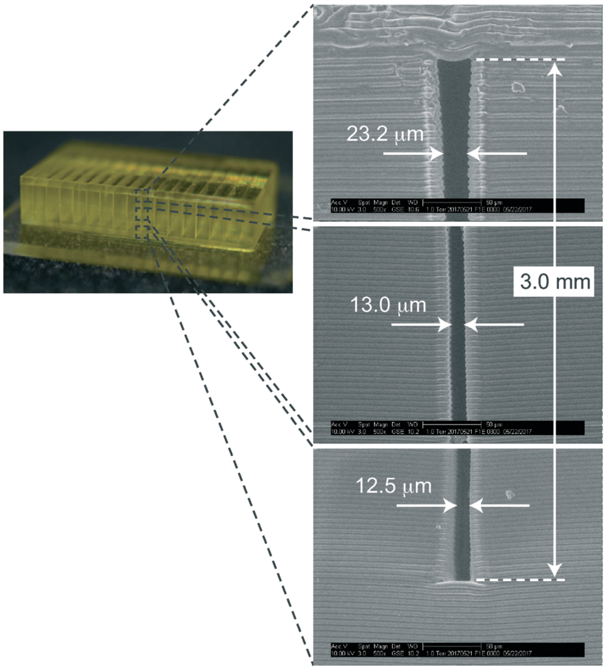

Fig. 8 Photograph and SEM images of 3D printed high aspect ratio flow channel.

$\Omega_{c,b}$ is less than or equal to ~0.1 and (2) the dose at the front of the channel, $\Omega_{tot,b}$ is such that it decays to less than or equal to ~1 at a distance of L_{min} above the bottom of the channel, where L_{min} is given by

$$L_{min} \approx -h_a \log(0.1) \tag{11}$$

$$= 2.3h_a. \tag{12}$$

Careful examination of the first 4 cases shown in Fig. 4(c) shows that these condition are fulfilled ($2.3h_a$ = 25 μm for 2% NPS), whereas for the last case the second condition is not fulfilled (Ω is ~1.7 at 25 μm).

The smallest possible channel height is realized when the designed channel is 3 layers thick with a height L_{min}, in which case the normalized layer thickness, ζ_l, is

$$\zeta_l = z_l/h_a \tag{13}$$

$$\approx 0.77. \tag{14}$$

Channels larger than this are possible with other layer thicknesses as long as conditions (1) and (2) are fulfilled.

To test whether this model is predictive, consider 3% NPS resin for which h_a = 8 μm, in which case

$$L_{min} = 2.3h_a = 18\ \mu m \tag{15}$$

$$z_l = L_{min}/3 = 6\ \mu m \tag{16}$$

$$\zeta_l = z_l/h_a = 0.75. \tag{17}$$

Fig. 5(a) shows the corresponding results where the 3 layer 18 μm channel is clearly open, as are 3 layer channels with 7 and 8 μm layers. The calculated normalized dose as a function of z in Fig. 5(b) clearly fulfills the model's conditions for all cases. As seen in the second row of SEM images in Fig. 5(a), increasing the channel height by adding more layers always results in open channels.

3.3.2 Channel width. The designed channel width for all of the cases presented so far is 4 pixels (30 μm). Consistent with our results in ref. 11, we found this to be the minimum channel width that gives 100% yield. However, the physical width of the channels in Fig. 4(a) and 5(a) are wider than the designed width by the equivalent of 1 to 2 pixels. This can be explained by noting that the Teflon film at the bottom of the resin tray is slightly cloudy. It therefore causes scattering of the light imaged through it, which broadens the effective exposure region of each pixel that is turned on. Lack of exposure for the pixels in the channel reduces the dose received at the edges of the channels to below the polymerization threshold.

We have developed a channel narrowing method that compensates for this lack of sufficient dose at channel edges. The left image in Fig. 6(a) shows a typical primary exposure pattern for a single layer containing a flow channel where white and black regions correspond to full exposure and no exposure, respectively. The right image is a second exposure of the same layer where only the 1 or 2 pixels adjacent to the channel are exposed. Fig. 6(b) and (c) show the effect of 1 and 2 pixel edge exposures for different exposure times for 2% and 3% NPS resin, respectively. This strategy is clearly very effective in narrowing the channel width, which is further illustrated in Fig. 6(d) where the measured channel width is plotted as a function of the edge exposure time. The width can be reduced from nearly 40 μm to 20 μm. As shown in Fig. 6(e), the edge dose has no effect on the channel height (as expected). The final result is that 18 μm × 20 μm channels can be consistently fabricated with 3% NPS resin.

3.4 Long channels

As an illustration of the efficacy of our approach, consider the fabrication of serpentine channels in Fig. 7 in 3% NPS resin with a 1 pixel 400 ms edge exposure. A microscope image of a single layer serpentine channel is shown in Fig. 7(a). Note the excellent optical clarity of imaging through the microscope slide substrate into the interior of the 3D printed device. A 3D serpentine channel design is shown in Fig. 7(b), with a photograph of a device containing 24 3D channels in Fig. 7(c). An SEM cross section is shown in Fig. 7(d). The channel is 41 mm long and occupies a volume of only 1.56 mm × 0.38 mm × 0.21 mm = 0.12 mm^3.

3.5 Tall high aspect ratio channel

As a further demonstration, consider the high aspect ratio channel shown in Fig. 8, fabricated with 5 μm layers, 4 pixels wide in 2% NPS with 2 pixel 400 ms edge exposure. Since we are not going for the minimum channel height, we can use a smaller layer thickness to decrease the sidewall surface relief that naturally occurs due to the layered nature of the 3D printing process. The channel width is <25 μm and its height is 3 mm (its length is 12 mm). Such channels are useful in nanoscale liposome synthesis for drug delivery as discussed in ref. 35.

4 Conclusions

In summary, we have shown that DLP-SLA is fully capable of 3D printing truly microfluidic flow channels with designed cross sectional areas as small as 18 μm × 20 μm. The out-of-plane void size is dependent on formulating a resin that adequately limits optical penetration during each layer exposure, which requires that the absorber's absorption spectrum fully cover the source spectrum. Small in-plane (*x*–*y*) void size is a function of the projected image resolution with a minimum width of 4 pixels. We have also shown that an additional edge dose for each layer containing a flow channel is an effective method of narrowing flow channel width. Taken together, these advances open the door for 3D printing to displace conventional microfluidic fabrication methods such as soft lithography.

Conflicts of interest

There are no conflicts of interest to declare.

Acknowledgements

We are grateful to the National Institutes of Health (R01 EB006124) for partial support of this work. We also thank Dr. Radim Knob for taking many of the SEM images.

References

1 A. K. Au, W. Huynh, L. F. Horowitz and A. Folch, *Angew. Chem.*, 2016, **128**, 3926–3946.

2 Y. He, Y. Wu, J.-Z. Fu, Q. Gao and J.-J. Qiu, *Electroanalysis*, 2016, **28**, 1658–1678.

3 R. Amin, S. Knowlton, A. Hart, B. Yenilmez, F. Ghaderinezhad, S. Katebifar, M. Messina, A. Khademhosseini and S. Tasoglu, *Biofabrication*, 2016, **8**, 022001.

4 N. Bhattacharjee, A. Urrios, S. Kang and A. Folch, *Lab Chip*, 2016, **16**, 1720–1742.

5 S. Waheed, J. M. Cabot, N. P. Macdonald, T. Lewis, R. M. Guijt, B. Paull and M. C. Breadmore, *Lab Chip*, 2016, **16**, 1993–2013.

6 C. Chen, B. T. Mehl, A. S. Munshi, A. D. Townsend, D. M. Spence and R. S. Martin, *Anal. Methods*, 2016, **8**, 6005–6012.

7 A. A. Yazdi, A. Popma, W. Wong, T. Nguyen, Y. Pan and J. Xu, *Microfluid. Nanofluid.*, 2016, **20**, 1–18.

8 C. M. B. Ho, S. H. Ng, K. H. H. Li and Y.-J. Yoon, *Lab Chip*, 2015, **15**, 3627–3637.

9 Y. Huang, M. C. Leu, J. Mazumder and A. Donmez, *J. Manuf. Sci. Eng.*, 2015, **137**, 014001.

10 B. C. Gross, J. L. Erkal, S. Y. Lockwood, C. Chen and D. M. Spence, *Anal. Chem.*, 2014, **86**, 3240–3253.
11 H. Gong, M. Beauchamp, S. Perry, A. T. Woolley and G. P. Nordin, *RSC Adv.*, 2015, **5**, 106621–106632.
12 M. J. Beauchamp, G. P. Nordin and A. T. Woolley, *Anal. Bioanal. Chem.*, 2017, 1–9.
13 R. D. Sochol, E. Sweet, C. C. Glick, S. Venkatesh, A. Avetisyan, K. F. Ekman, A. Raulinaitis, A. Tsai, A. Wienkers, K. Korner, K. Hanson, A. Long, B. J. Hightower, G. Slatton, D. C. Burnett, T. L. Massey, K. Iwai, L. P. Lee, K. S. J. Pister and L. Lin, *Lab Chip*, 2016, **16**, 668–678.
14 R. Walczak and K. Adamski, *J. Micromech. Microeng.*, 2015, **25**, 085013.
15 Y. Ukita, Y. Takamura and Y. Utsumi, *Jpn. J. Appl. Phys.*, 2016, **55**, 06GN02.
16 A. I. Shallan, P. Smejkal, M. Corban, R. M. Guijt and M. C. Breadmore, *Anal. Chem.*, 2014, **86**, 3124–3130.
17 J. M. Lee, M. Zhang and W. Y. Yeong, *Microfluid. Nanofluid.*, 2016, **20**, 5.
18 L. Donvito, L. Galluccio, A. Lombardo, G. Morabito, A. Nicolosi and M. Reno, *J. Micromech. Microeng.*, 2015, **25**, 035013.
19 C. I. Rogers, K. Qaderi, A. T. Woolley and G. P. Nordin, *Biomicrofluidics*, 2015, **9**, 1–9.
20 N. P. Macdonald, J. M. Cabot, P. Smejkal, R. M. Guijt, B. Paull and M. C. Breadmore, *Anal. Chem.*, 2017, **89**, 3858–3866.
21 K. G. Lee, K. J. Park, S. Seok, S. Shin, J. Y. Park, Y. S. Heo, S. J. Lee and T. J. Lee, *et al.*, *RSC Adv.*, 2014, **4**, 32876–32880.
22 K. B. Anderson, S. Y. Lockwood, R. S. Martin and D. M. Spence, *Anal. Chem.*, 2013, **85**, 5622–5626.
23 P. S. Venkateswaran, A. Sharma, S. Dubey, A. Agarwal and S. Goel, *IEEE Sens. J.*, 2016, **16**, 3000–3007.
24 H. N. Chan, Y. Shu, B. Xiong, Y. Chen, Y. Chen, Q. Tian, S. A. Michael, B. Shen and H. Wu, *ACS Sens.*, 2015, **1**, 227–234.
25 A. Urrios, C. Parra-Cabrera, N. Bhattacharjee, A. M. Gonzalez-Suarez, L. G. Rigat-Brugarolas, U. Nallapatti, J. Samitier, C. A. DeForest, F. Posas and J. L. Garcia-Cordero, *et al.*, *Lab Chip*, 2016, **16**, 2287–2294.
26 G. W. Bishop, J. E. Satterwhite-Warden, I. Bist, E. Chen and J. F. Rusling, *ACS Sens.*, 2015, **1**, 197–202.
27 K. C. Bhargava, B. Thompson and N. Malmstadt, *Proc. Natl. Acad. Sci. U. S. A.*, 2014, **111**, 15013–15018.
28 W. G. Patrick, A. A. Nielsen, S. J. Keating, T. J. Levy, C.-W. Wang, J. J. Rivera, O. Mondragón-Palomino, P. A. Carr, C. A. Voigt and N. Oxman, *et al.*, *PLoS One*, 2015, **10**, e0143636.
29 J. M. Zhang, E. Q. Li, A. A. Aguirre-Pablo and S. T. Thoroddsen, *RSC Adv.*, 2016, **6**, 2793–2799.
30 A. J. Morgan, L. H. San Jose, W. D. Jamieson, J. M. Wymant, B. Song, P. Stephens, D. A. Barrow and O. K. Castell, *PLoS One*, 2016, **11**, e0152023.
31 H. Gong, A. T. Woolley and G. P. Nordin, *Lab Chip*, 2016, **16**, 2450–2458.
32 C. I. Rogers, J. V. Pagaduan, G. P. Nordin and A. T. Woolley, *Anal. Chem.*, 2011, **83**, 6418–6425.
33 A. Urrios, C. Parra-Cabrera, N. Bhattacharjee, A. M. Gonzalez-Suarez, L. G. Rigat-Brugarolas, U. Nallapatti, J. Samitier, C. A. DeForest, F. Posas, J. L. Garcia-Cordero and A. Folch, *Lab Chip*, 2016, 1–8.
34 L. Láng, *Absorption Spectra in the Ultraviolet and Visible Region*, Academic Press, 1961.
35 R. R. Hood and D. L. DeVoe, *Small*, 2015, **11**, 5790–5799.